NASA/TM-20240006582

Mechanisms of Apatite Formation in Reactions of $Yb_{2-2x}Gd_{2x}Si_2O_7$ With CMAS

Jamesa L. Stokes and Bryan J. Harder
Glenn Research Center, Cleveland, Ohio

Valerie L. Wiesner
Langley Research Center, Hampton, Virginia

Douglas E. Wolfe
The Pennsylvania State University, University Park, Pennsylvania

June 2024

NASA STI Program Report Series

Since its founding, NASA has been dedicated to the advancement of aeronautics and space science. The NASA scientific and technical information (STI) program plays a key part in helping NASA maintain this important role.

The NASA STI program operates under the auspices of the Agency Chief Information Officer. It collects, organizes, provides for archiving, and disseminates NASA's STI. The NASA STI program provides access to the NTRS Registered and its public interface, the NASA Technical Reports Server, thus providing one of the largest collections of aeronautical and space science STI in the world. Results are published in both non-NASA channels and by NASA in the NASA STI Report Series, which includes the following report types:

- TECHNICAL PUBLICATION.
  Reports of completed research or a major significant phase of research that present the results of NASA Programs and include extensive data or theoretical analysis. Includes compilations of significant scientific and technical data and information deemed to be of continuing reference value. NASA counterpart of peer-reviewed formal professional papers but has less stringent limitations on manuscript length and extent of graphic presentations.

- TECHNICAL MEMORANDUM.
  Scientific and technical findings that are preliminary or of specialized interest, e.g., quick release reports, working papers, and bibliographies that contain minimal annotation. Does not contain extensive analysis.

- CONTRACTOR REPORT.
  Scientific and technical findings by NASA-sponsored contractors and grantees.

- CONTRACTOR REPORT.
  Scientific and technical findings by NASA-sponsored contractors and grantees.

- CONFERENCE PUBLICATION.
  Collected papers from scientific and technical conferences, symposia, seminars, or other meetings sponsored or co-sponsored by NASA.

- SPECIAL PUBLICATION.
  Scientific, technical, or historical information from NASA programs, projects, and missions, often concerned with subjects having substantial public interest.

- TECHNICAL TRANSLATION.
  English-language translations of foreign scientific and technical material pertinent to NASA's mission.

Specialized services also include organizing and publishing research results, distributing specialized research announcements and feeds, providing information desk and personal search support, and enabling data exchange services.

For more information about the NASA STI program, see the following:

- Access the NASA STI program home page at http://www.sti.nasa.gov

NASA/TM-20240006582

Mechanisms of Apatite Formation in Reactions of $Yb_{2-2x}Gd_{2x}Si_2O_7$ With CMAS

Jamesa L. Stokes and Bryan J. Harder
Glenn Research Center, Cleveland, Ohio

Valerie L. Wiesner
Langley Research Center, Hampton, Virginia

Douglas E. Wolfe
The Pennsylvania State University, University Park, Pennsylvania

National Aeronautics and
Space Administration

Glenn Research Center
Cleveland, Ohio 44135

June 2024

This work was sponsored by the
Transformative Aeronautics Concepts Program.

Level of Review: This material has been technically reviewed by technical management.

This report is available in electronic form at https://www.sti.nasa.gov/ and https://ntrs.nasa.gov/

NASA STI Program/Mail Stop 050
NASA Langley Research Center
Hampton, VA 23681-2199

Mechanisms of Apatite Formation in Reactions of $Yb_{2-2x}Gd_{2x}Si_2O_7$ With CMAS

Jamesa L. Stokes and Bryan J. Harder
National Aeronautics and Space Administration
Glenn Research Center
Cleveland, Ohio 44135

Valerie L. Wiesner
National Aeronautics and Space Administration
Langley Research Center
Hampton, Virginia 23681

Douglas E. Wolfe
The Pennsylvania State University
University Park, Pennsylvania 16802

Abstract

Bulk β-$Yb_{1.9}Gd_{0.1}Si_2O_7$, β-$Yb_{1.6}Gd_{0.4}Si_2O_7$, and γ-$Yb_{1.4}Gd_{0.6}Si_2O_7$, along with baseline γ-$Y_2Si_2O_7$ and β-$Yb_2Si_2O_7$ were investigated in contact with a molten silicate to determine mechanisms of thermochemical degradation. A model 30.67CaO-8.25MgO-12.81$AlO_{1.5}$-48.27SiO_2 silicate composition was deposited on the surfaces of the samples at a loading of ~2 mg/cm^2. Reactions with the molten silicate resulted in the formation of a silicate apatite layer, which has been shown to reduce further molten silicate infiltration. Additions of gadolinium up to 30 mol% to $Yb_2Si_2O_7$ reduced infiltration up to ~60% compared to baseline $Yb_2Si_2O_7$, but additional exposure time at temperature resulted in loss of the apatite layer. The results herein indicate that doping with gadolinium disilicate may not be beneficial in the long term degradation of disilicate-based EBCs by molten silicates.

Introduction

Rare earth (RE) disilicates are often used as topcoat materials in environmental barrier coating (EBC) systems to protect silicon carbide (SiC)-based ceramic matrix composites (CMCs) against water-vapor induced corrosion in gas turbine engines (Refs. 1 to 3). RE disilicates with small cations such as ytterbium disilicate ($Yb_2Si_2O_7$) exhibit crystal structures that have a similar thermal expansion coefficient (CTE) to that of SiC-based CMCs (~4 to 4.5×10^{-6}/K) and have fairly good resistance against water vapor ingress (Refs. 4 to 6). However, EBC materials must also be able to withstand a host of other damage mechanisms in the engine environment, including water-vapor induced volatility, salt corrosion, thermomechanical stresses, particulate erosion and foreign object damage, and corrosion by molten deposits of ingested dust particles (Ref. 7).

With the rise in the inlet temperature of gas turbine engines exceeding ~1200 °C, the degradation of coatings by ingested particulates has become an eminent concern when selecting prospective materials for topcoat use (Refs. 8 and 9). These particles are primarily composed of CaO, MgO, Al_2O_3, and SiO_2 (CMAS) oxides that can quickly become molten when introduced to the hot section of jet engines and dissolve coating materials, which may result in the precipitation of extraneous phases. Moreover, the ingress of molten deposits can occur via grain boundaries and interconnected porosity in the coating.

Once infiltration happens, these deposits can resolidify upon cooling, resulting in coating stiffening and a reduction in strain tolerance. CTE mismatch of the resolidified glass with the coating is also of concern (Refs. 10 and 11).

Reactive crystallization of CMAS has been proposed by several authors in the literature as a mechanism by which to reduce melt infiltration (Ref. 12). A number of authors have evaluated inducing crystallization of CMAS as a protection method (Refs. 13 and 14). This method of CMAS mitigation relies on the rapid reaction of CMAS with RE-containing coatings to sequester melt components into equilibrium phases that will form a barrier layer against further ingress. Specifically, the formation of a $Ca_2RE_8(SiO_4)_6O_2$ silicate apatite utilizes both CaO and SiO_2 from CMAS, thereby reducing overall melt volume for interactions with RE-zirconate materials. The stability of apatite is largely dependent on RE cation size (Refs. 15 and 16), and past findings have demonstrated the reduced propensity of $Yb_2Si_2O_7$ to form apatite with CMAS due to smaller cation size and incorporation of SiO_2 from the disilicate into the melt (Refs. 17 to 22). The reduced apatite formation observed for smaller RE cations results from the need for more dissolved coating material to achieve thermodynamic stability of the apatite phase (Ref. 23). In studies of RE zirconates exposed to CMAS, it was observed that larger RE cations were more beneficial in promoting crystallization (Refs. 24 and 25). However, RE disilicates with larger RE cations like gadolinium exhibit polymorphism with temperature and have CTEs much greater (~8 to 14×10^{-6}/K) than ideal for EBCs (Refs. 6 and 26).

In consideration of the benefits of both small and large RE cations, recent studies have focused on preparing solid solutions of disilicate materials to tune their thermal expansion and thermal conductivity (Refs. 27 to 30). However, few studies have systematically investigated the effects of the cation type and amount in disilicate solid solutions on apatite formation and CMAS reactivity. He et al. investigated a four-component disilicate-monosilicate composite coating and found that CMAS infiltration was dramatically reduced (Ref. 31). However, this reduction was primarily attributed to the reaction of the monosilicate with SiO_2 at grain boundaries to form additional disilicate, reducing open pathways for infiltration. Chen et al. investigated four, five, and six-component disilicate systems in contact with CMAS for comparison to ytterbium and yttrium disilicate; the authors found that an increase in the average cation size of the solid solutions resulted in increased apatite formation and reduced CMAS infiltration compared to the single-component (Yb, Y) disilicates (Ref. 32). However, to date, there has been no significant investigation on how various elements in the multicomponent systems react and form apatite or other reaction products. There has not been any discussion on the primary cations needed to drive crystallization in these multicomponent systems. This report details investigations of $Yb_{2-2x}Gd_{2x}Si_2O_7$ reactions with CMAS to fundamentally understand the role of mixed small and large RE disilicates in the formation of apatite as compared to single-component RE disilicates.

Materials and Methods

Ytterbium disilicate ($Yb_2Si_2O_7$, YbDS) and yttrium disilicate ($Y_2Si_2O_7$, YDS) were chosen as the single-component disilicates to compare to $Yb_{2-2x}Gd_{2x}Si_2O_7$ solid solutions. Starting YbDS and YDS powders were obtained from Praxair, Inc. (99.9%). The as-received powders were heat treated at 1600 °C for 10 h to ensure phase purity. YbDS exhibited the β-$RE_2Si_2O_7$ *C*2/*m* structure, and YDS exhibited the γ-$RE_2Si_2O_7$ $P2_1/c$ structure, which were the thermodynamically expected phases. Gd_2O_3 (HEFA Rare Earth Canada, Inc., 99.99%), and SiO_2 (Alfa Aesar, 99.5%) were used to synthesize gadolinium disilicate ($Gd_2Si_2O_7$, GdDS). The powders were mixed in their respective weight ratios and ball milled in ethanol with 10 mm spherical ZrO_2 milling media for 24 h. The mixed powders were heat treated at 1600 °C for 10 h to form phase pure GdDS. Solid solutions of $Yb_{2-2x}Gd_{2x}Si_2O_7$ were fabricated using the synthesized

YbDS and GdDS single-phase powders via a mixing and heat treatment procedure similar to that outlined above. In previous studies on the stability of $Yb_{2-2x}Gd_{2x}Si_2O_7$ solid solutions, YbDS was shown to accommodate substitutions of up to ~30 mol% GdDS before phase segregation would occur (Ref. 33). Thus, 5 mol% (β-$Yb_{1.9}Gd_{0.1}Si_2O_7$), 20 mol% (β-$Yb_{1.6}Gd_{0.4}Si_2O_7$), and 30 mol% (γ-$Yb_{1.4}Gd_{0.6}Si_2O_7$) additions of GdDS were chosen to evaluate the effect of cation doping on apatite formation in single-phase solid solutions. The $Yb_{2-2x}Gd_{2x}Si_2O_7$, YbDS, and YDS powders were pressed into ~1 g, 12.7 mm diameter pellets and heat treated at 1600 °C for 6 h in air to obtain ~95% density (as measured via Archimedes method).

The outer surfaces of the prepared pellets were polished to a 1 μm finish prior to CMAS application to minimize the effects of surface roughness. A 30.67CaO-8.25MgO-12.81$AlO_{1.5}$-48.27SiO_2 CMAS composition was prepared by solid-state synthesis using $CaCO_3$ (>99%, Alfa Aesar), MgO (99.95%, Cerac, Inc.), Al_2O_3 (>99%, Almatis, Inc.), and SiO_2 (99.5%, Alfa Aesar) powders; the mixed powders were melted in a platinum crucible at 1500 °C for 1 h to obtain a glass (Ref. 34). The CMAS glass was ground into a fine powder and sprayed onto a 6.35 mm diameter area of the pellet surface using an airbrush procedure detailed in previous studies (Refs. 35 and 36). The CMAS loading was ~2 mg/cm^2. Samples loaded with CMAS were then heat treated in a stagnant air box furnace at 1400 °C for times of 10 min, 1 h, or 4 h. Phase constitution was assessed via X-ray diffraction (XRD) with copper radiation (Cu Kα = 1.541Å) using a D8 Advance (Bruker Corporation) diffractometer. Reaction products and microstructural features were characterized by scanning electron microscopy (SEM) (Hitachi S4700, Phenom ProX). Compositional analysis of the reaction products was carried out using energy dispersive spectroscopy (EDS).

Results

CMAS Corrosion of γ-YDS

Figure 1(a) displays the XRD scans of YDS after CMAS exposure. Apatite was observed after only 10 min at 1400 °C. The XRD scans at 10 min, 1 h, and 4 h were identical, with no changes observed in the intensities of apatite or γ-YDS peaks. The reflection planes of the apatite structure are noted by the black hexagons in the XRD scans. In randomly oriented apatite, the (211) plane (~32.1°) exhibits the highest peak intensity (Ref. 37). However, for YDS exposed to CMAS, the (002) plane (~26.3°) of the formed apatite exhibited the highest intensity after 10 min to 4 h, possibly indicating that the fastest growth direction of the apatite phase was perpendicular to the {001} family of planes, the basal plane of this crystal structure (Ref. 15). SEM analysis of the apatite phase indicated that needle like-precipitates had formed on the surface of YDS after 10 min (Figure 1(b)), which agrees with XRD observations of a [001] growth direction, as the c-axis is elongated in this crystal structure.

As shown in Figure 1(b), the layer of apatite formed after 10 min was composed of needles and was ~50 μm thick; the needles were densely packed with pockets of residual CMAS between them. The amount of CMAS remaining on the surface of the samples above the interaction/apatite layer was also tracked to determine infiltration behavior. After 10 min at 1400 °C (Figure 1(b)), there was an ~83 μm thick layer of CMAS remaining at the surface, whereas only ~4 μm of CMAS was observed at the surface after 4 h (Figure 1(d)). The nominal composition of the apatite precipitates was $Ca_2Y_8(SiO_4)_6O_2$, which is consistent with previous reports on the reaction of YDS with this CMAS composition (Refs. 17, 38, and 39). After 1 h of exposure (Figure 1(c)), the thickness of the interaction layer decreased by approximately 10%; noticeable coarsening of the apatite grains was observed. The apatite layer after 4 h of exposure was of similar thickness to that after 1 h of exposure (Figure 1(d)); however, there was less residual CMAS remaining on the surface of the sample. This indicates that while apatite formed as a reaction product

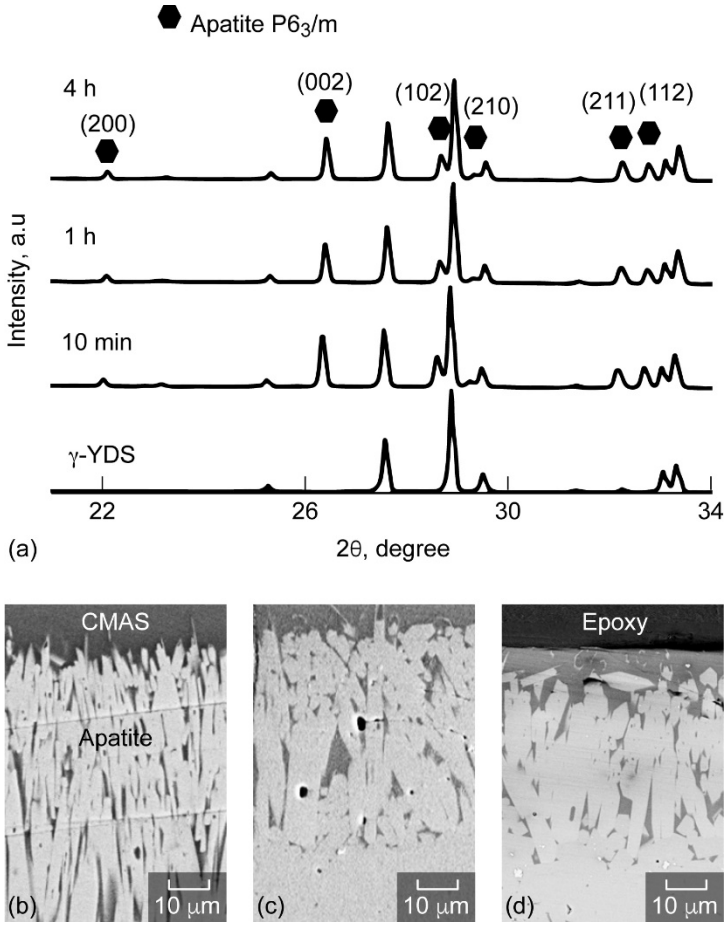

Figure 1.—(a) XRD scans of YDS as synthesized and after CMAS exposure. SEM micrographs of YDS after CMAS exposure at 1400 °C for (b) 10 min, (c) 1 h, and (d) 4 h. The apatite phase peaks are marked with hexagonal symbols. All other peaks are attributed to γ-YDS.

between CMAS and YDS, remaining CMAS was able to continue to penetrate the coating at 1400 °C. Such behavior is in line with observations of the complete consumption of yttrium disilicate by CMAS to form apatite, as CaO, which aids in apatite formation, is depleted and halts the driving force for further apatite precipitation (Refs. 38 and 40). Additionally, dissolution of RE disilicate results in incorporation of SiO_2 from the material into the melt. This results in a decrease in the CaO/SiO_2 ratio of the melt, shifting the thermodynamic equilibrium so that apatite crystallization is reduced.

CMAS Corrosion of YbDS, $Yb_{1.9}Gd_{0.1}Si_2O_7$, and $Yb_{1.6}Gd_{0.4}Si_2O_7$

The XRD scans of YbDS after exposure to CMAS are shown in Figure 2(a). The reaction of YbDS with CMAS also resulted in the formation of apatite. Similar to YDS, some texturing of the apatite phase was observed, although the texture favored the (200) plane (~22.2°), indicating that the elongated dimension of the apatite phase was aligning primarily parallel to the sample surface as it crystallized. After the initial formation of apatite by 10 min, the apatite peak intensities decreased with time. The morphology of the apatite precipitates for YbDS was remarkedly different from that of the precipitates for YDS, as shown after 10 min in Figure 2(b). The apatite precipitates formed within the melt were largely

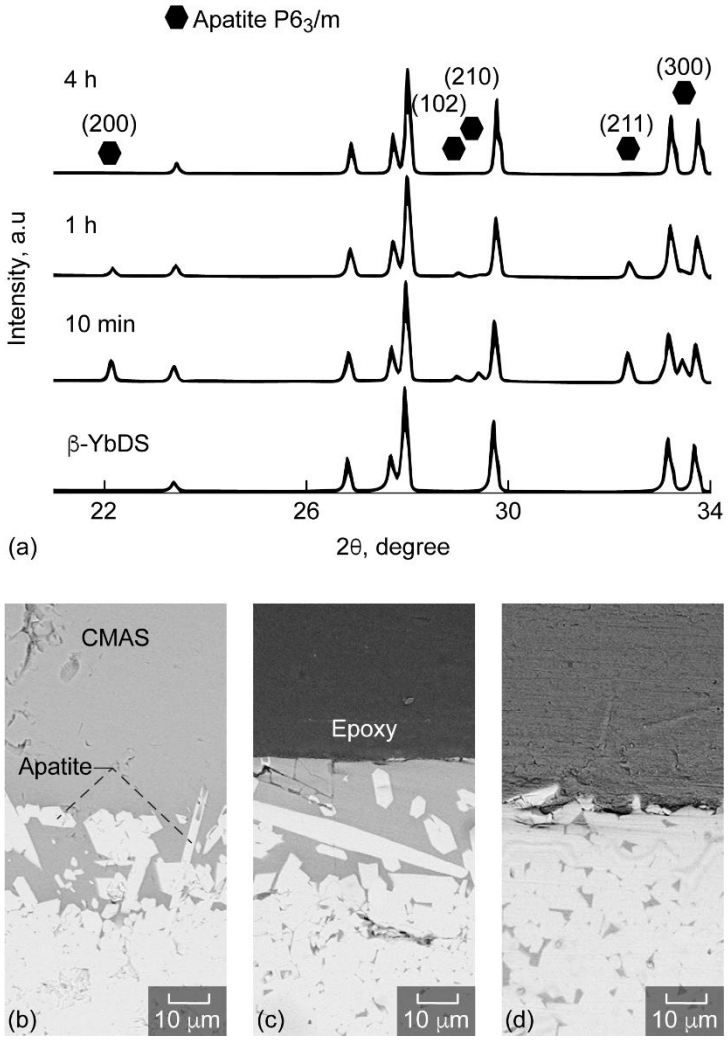

Figure 2.—(a) XRD scans of YbDS as synthesized and after CMAS exposure. SEM micrographs of YbDS after CMAS exposure at 1400 °C for (b) 10 min, (c) 1 h, and (d) 4 h. The apatite phase peaks are marked with hexagonal symbols. All other peaks are attributed to β-YbDS.

detached from the YbDS surface. Instead of continuous elongated needles, isolated precipitates of the basal plane and other orientations of the apatite structure were observed. Smaller precipitates found directly at the CMAS-YbDS interface were primarily composed of YbDS grains. As in the YDS samples, the apatite precipitates also had a Ca/RE ratio of 1:4 ($Ca_2Yb_8(SiO_4)_6O_2$). There was ~44 μm of residual CMAS on the surface of YbDS after 10 min, ~50% lower than seen for YDS after the same exposure time. After 1 h (Figure 2(c)), the amount of CMAS remaining above the interaction layer decreased to ~6 μm in thickness, although some apatite formation was still observed. Pockets of CMAS were observed between grains well below the surface of YbDS, indicating that CMAS continued to infiltrate the sample.

Similar behavior was observed after 4 h of exposure, in which there was no CMAS remaining on the surface of YbDS. No apatite was observed at the sample surface after 4 h (Figure 2(d)), which correlated with the decrease in apatite peak intensities observed in the XRD data. The composition of apatite remained constant at all exposure times in which apatite was observed.

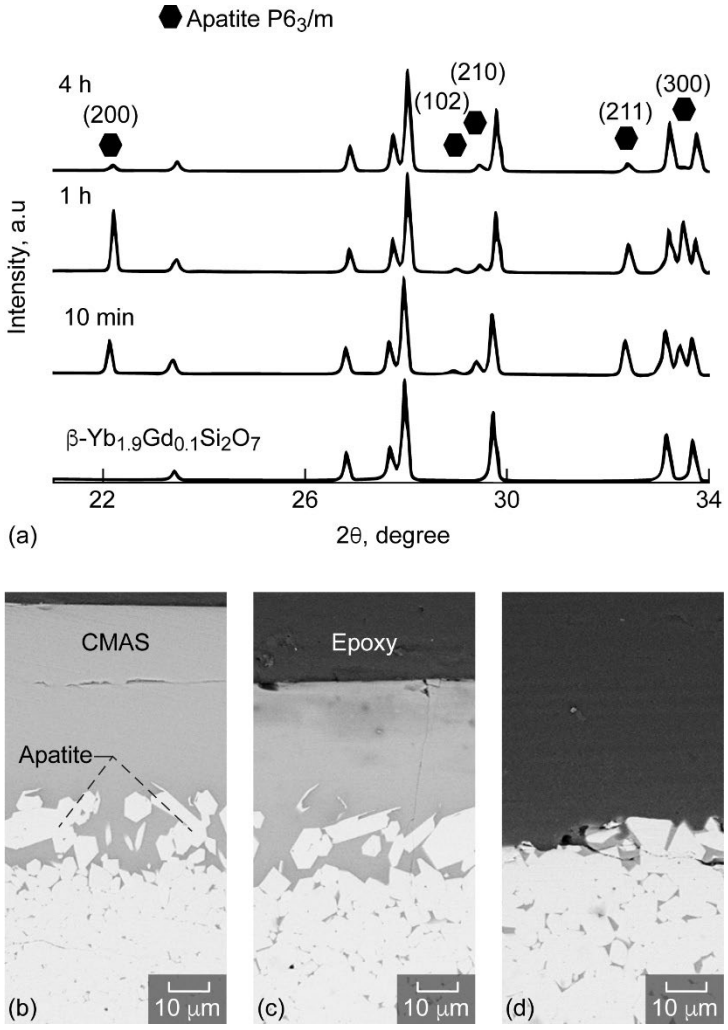

Figure 3.—(a) XRD scans of $Yb_{1.9}Gd_{0.1}Si_2O_7$ as synthesized and after CMAS exposure. SEM micrographs of YDS after CMAS exposure at 1400 °C for (b) 10 min, (c) 1 h, and (d) 4 h. All other peaks are attributed to β-$Yb_{1.9}Gd_{0.1}Si_2O_7$.

For $Yb_{1.9}Gd_{0.1}Si_2O_7$ (5 mol% GdDS), the morphology of the formed apatite closely resembled that seen for YbDS. As shown in the XRD data (Figure 3(a)), the intensity of the (200) reflection of apatite after 1 h of exposure was twice as high as the intensity observed after 10 min. It is important to note that molten CMAS, as an amorphous material, can reduce the signal-to-noise ratio of crystalline materials in XRD data. CMAS fully infiltrated the $Yb_{1.9}Gd_{0.1}Si_2O_7$ sample at 1400 °C within 4 h. The apatite formed after 10 min (Figure 3(b)) and 1 h (Figure 3(c)) appeared similar in size and morphology; thus, the increase in peak intensity after 1 h could be attributed to an increase in peak signal from the surface as CMAS infiltrated the sample.

After 4 h, apatite peaks were largely absent from the XRD data and no residual CMAS remained on the surface of the sample (Figure 3(d)). EDS data did not show any significant changes in the apatite composition between 10 min and 4 h. The formed apatite contained both Gd^{3+} and Yb^{3+} and had a nominal composition of $Ca_2Yb_{7.5}Gd_{0.5}(SiO_4)_6O_2$.

In the case of $Yb_{1.6}Gd_{0.4}Si_2O_7$ (20 mol% GdDS), the morphology of the apatite precipitates resembled a mixture of those observed for YDS and YbDS. After 10 min of exposure (Figure 4(a)), longer needle-

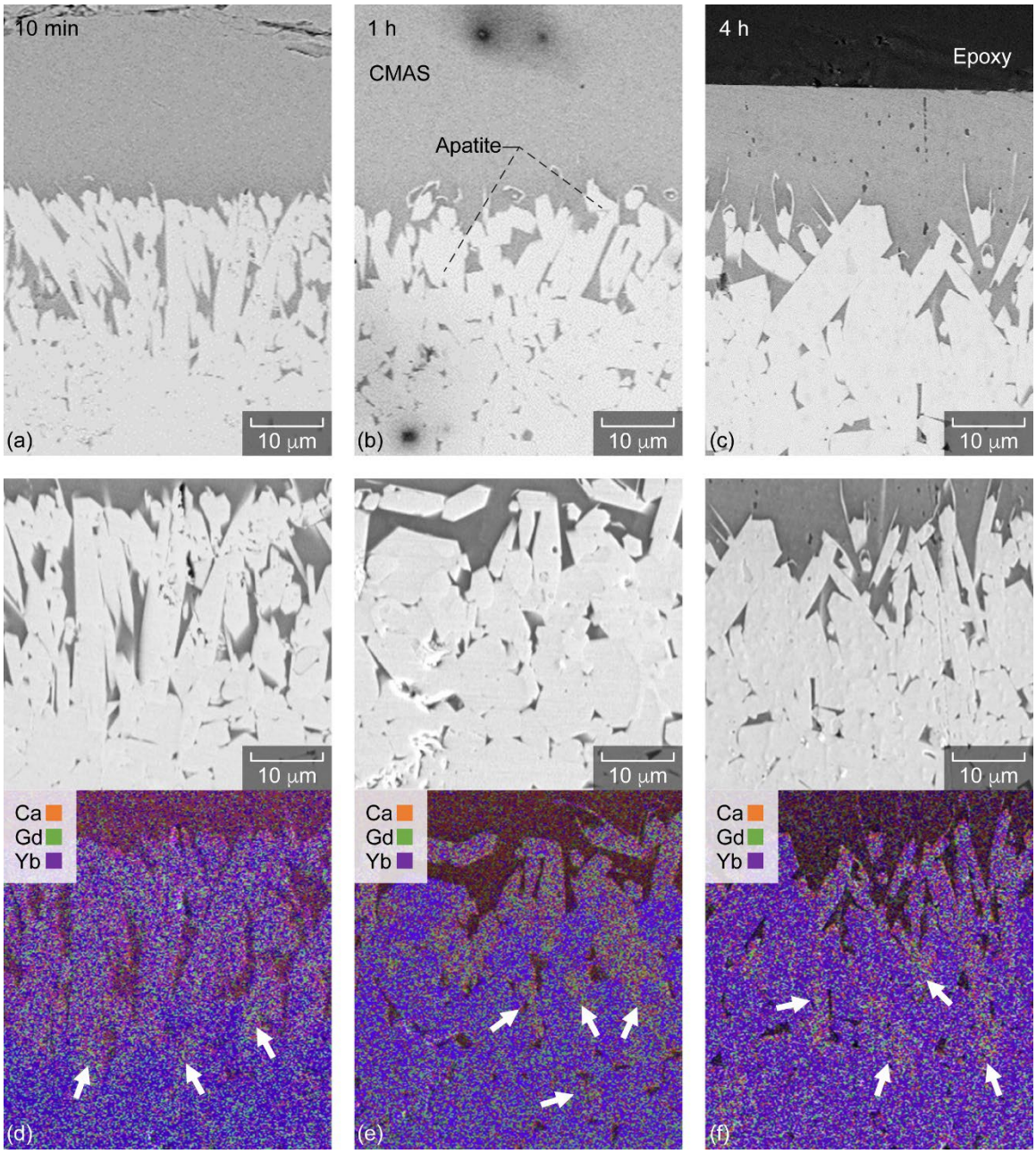

Figure 4.—SEM micrographs of the interaction layer between β-$Yb_{1.6}Gd_{0.4}Si_2O_7$ and CMAS at 1400 °C after (a) and (d) 10 min, (b) and (e) 1 h, and (c) and (f) 4 h, with compositional maps from EDS showing the distribution of Ca (orange), Yb (purple), and Gd (green). Arrows indicate the location of apatite precipitates beneath the original sample surface.

like precipitates were seen oriented normal to the surface and interspersed with precipitates oriented parallel to the surface. There was a similar amount of CMAS remaining at the surface (~56 μm) after 10 min and 1 h (Figure 4(b)). EDS analysis showed that apatite precipitates had formed within the bulk material below the interaction layer after 1 h (Figure 4(b) and (e)), indicating that CMAS had infiltrated into $Yb_{1.6}Gd_{0.4}Si_2O_7$. After 4 h (Figure 4(c)), with further CMAS infiltration, the apatite precipitates at the surface appeared to decrease in size, while the amount of apatite observed in regions below the surface (Figure 4(f)) increased. The amount of CMAS at the surface also decreased, as the measured residual thickness was ~25 μm, approximately half of the thickness observed after 10 min and 1 h. Gd^{3+} and

Yb^{3+} were both incorporated in the apatite phase ($Ca_2Yb_6Gd_2(SiO_4)_6O_2$)), which is consistent with the $Yb_{1.9}Gd_{0.1}Si_2O_7$ composition. The apatite chemistry did not change over the exposure time.

CMAS Corrosion of $Yb_{1.4}Gd_{0.6}Si_2O_7$

XRD of the CMAS-exposed $Yb_{1.4}Gd_{0.6}Si_2O_7$ (30 mol% GdDS) (Figure 5(a)) showed that the peaks associated with apatite and their intensities remained consistent between 10 min and 4 h. After 10 min, a peak reflection not attributed to either apatite or γ-$RE_2Si_2O_7$ was observed at ~28°. The intensity of this peak increased with exposure time and was identified as the primary peak reflection (021) of β-$RE_2Si_2O_7$, which precipitated from the interaction of $Yb_{1.4}Gd_{0.6}Si_2O_7$ with CMAS. Micrographs of the interaction layer showed that there was an increased number of apatite precipitates at the surface as compared to the materials with lower GdDS contents. The interaction layer containing apatite increased in thickness with time, which is in contrast to the other materials in this study. The needles appeared to be thicker than the apatite grains formed with YDS; however, there was less CMAS left on the surface (~54 μm) compared to YDS after 10 min (Figure 5(b) and (e)). EDS maps indicated a region of precipitates directly below the surface apatite layer that was Gd-deficient. This region likely corresponds to the β-$RE_2Si_2O_7$ phase, which was observed via XRD. This precipitate layer (referred to as the β layer) was measured to be ~11 μm thick after 10 min. After 1 h (Figure 5(c) and (f)), both the interaction zone and β layer doubled in size. As with $Yb_{1.6}Gd_{0.4}Si_2O_7$, the apatite precipitates grew into the bulk. After 4 h (Figure 5(d) and (g)), the β precipitates coarsened, nearly surrounding the apatite. The apatite composition was nominally constant after all exposure times as $Ca_2Yb_5Gd_3(SiO_4)_6O_2$, containing both Gd^{3+} and Yb^{3+}. The β layer precipitate composition also remained nominally consistent as $Yb_{1.6}Gd_{0.4}Si_2O_7$ and contained 33% less GdDS than the starting disilicate. There was ~35 μm of CMAS remaining at the surface after 4 h, although no large pockets of CMAS were seen much further below the interaction region observed after 1 h.

Discussion

The thermochemical interactions of Gd-doped YbDS with CMAS produced mixed precipitate morphologies that resembled the apatite formed between CMAS and phase pure YDS and/or YbDS. Reactions of the CMAS with YDS resulted in a continuous, highly textured apatite layer, whereas a discontinuous, primarily randomly-oriented apatite was formed in reactions with YbDS. XRD of the initial pellet surfaces indicated no preferential orientation of the surface, although this could be attributed to the varying surface energies of the planes of the initial crystal structures.

The preferred growth of apatite could therefore be influenced by diffusion and transport of participating oxide species across the CMAS-apatite interface. Many studies on the structure of Ca-RE apatite solid solutions have shown that shared Ca/RE sites in the apatite structure are arranged parallel to the c-axis of the crystal, normal to the basal plane (Refs. 15 and 16). In this study, as CMAS reacted with YDS, needle growth probably proceeded as apatite was formed with Y^{3+} incorporated at these sites. In the GdDS-doped YbDS materials with low (<10%) GdDS content, there was no continuous reaction layer observed.

Instead, the apatite precipitates were detached from the original surface and suspended in the residual melt. In the case of phase-pure YbDS, YbDS grains seemed to be dislodged at the CMAS-YbDS interface after the initial formation of apatite. In these reactions, CMAS continued to infiltrate the material via grain boundaries (as evidenced by pockets of CMAS found between grains). YbDS grains may dislodge from the bulk material or YbDS may dissolve and then reprecipitate in the same location as the infiltrating CMAS. Either way, this behavior, coupled with the lack of a continuous interaction layer,

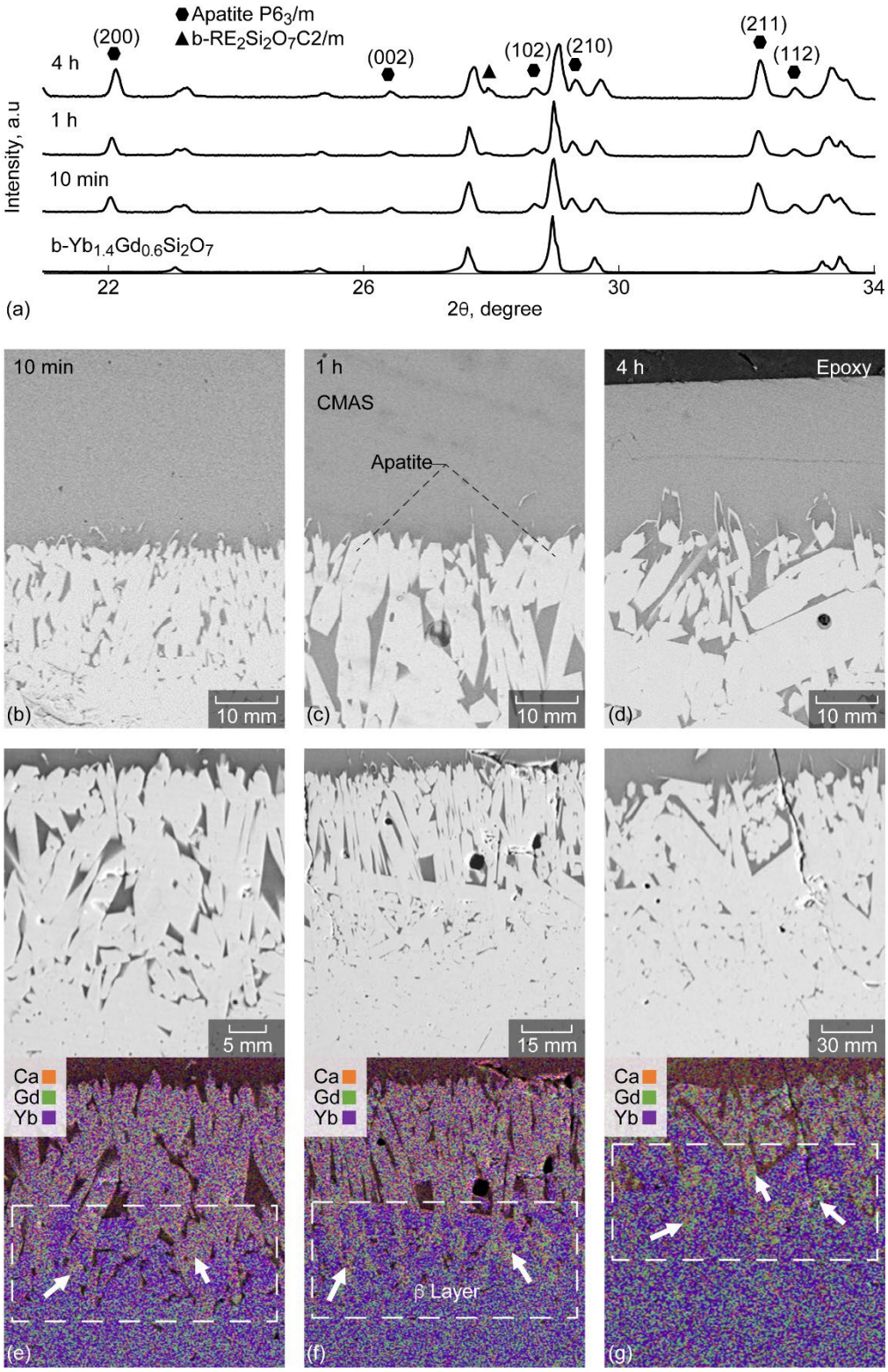

Figure 5.—(a) XRD scans of $Yb_{1.4}Gd_{0.6}Si_2O_7$ as synthesized and after CMAS exposure. SEM micrographs of the reaction zone between $Yb_{1.4}Gd_{0.6}Si_2O_7$ and CMAS at 1400 °C after (b) and (e) 10 min, (c) and (f) 1 h, and (d) and (g) 4 h, with compositional maps from EDS showing the distribution of Ca (orange), Yb (purple), and Gd (green). Arrows indicate the location of apatite precipitates beneath the original sample surface. The white dashed rectangle indicates the location of the β phase layer.

indicates that the speed at which CMAS infiltrates YbDS may be substantially faster than the formation of apatite. Dislodging and separation of YbDS grains may be why apatite precipitates were suspended in the residual melt. If CMAS infiltrates and dislodges YbDS grains immediately upon contact, YbDS grains will migrate into the melt. The increased surface area of YbDS in the CMAS melt may change the localized thermal equilibria and drive the nucleation of apatite precipitates. The displacement of randomly oriented grains from the surface to nucleate apatite would also support the limited basal plane texturing observed for apatite grown in the YbDS-containing materials.

Since the apatite structure is more thermodynamically stable with larger RE cations, it was expected that Gd^{3+} would be preferentially incorporated in the formed apatite over Yb^{3+} (Refs. 41 and 42). However, as observed for the 20 and 30 mol% GdDS-doped samples, Gd^{3+} and Yb^{3+} were incorporated into apatite in approximately equivalent ratios to the starting materials. With only 5 mol% GdDS ($Yb_{1.9}Gd_{0.1}Si_2O_7$), the morphology of the apatite formed closely matched that for phase-pure YbDS. No benefit in infiltration resistance or apatite formation was noted using this small amount of GdDS, as CMAS fully penetrated the material (no residual CMAS was observed at the surface after 4 h). A GdDS content of 20 mol% promoted quicker apatite formation and reduced CMAS infiltration over the same amount of time. However, in this material, the apatite grains diffused inwards as CMAS infiltrated along grain boundaries. Increasing the GdDS content to 30 mol% resulted in increased apatite formation and reduced CMAS infiltration. At this GdDS concentration, the reaction to form apatite caused destabilization of the γ-$RE_2Si_2O_7$ structure of $Yb_{1.4}Gd_{0.6}Si_2O_7$, even though Gd^{3+} and Yb^{3+} were utilized equally with respect to their ratio in the initial material The grains in the β layer were deficient in Gd and had the same composition as $Yb_{1.6}Gd_{0.4}Si_2O_7$. Such a result suggests that this YbDS-GdDS solid solution is more energetically stable than $Yb_{1.4}Gd_{0.6}Si_2O_7$ in contact with the CMAS composition studied. The incorporation of Yb^{3+} into the apatite phase indicates that the $Yb_{1.4}Gd_{0.6}Si_2O_7$ grains dissolved in the CMAS as opposed to preferential extraction of GdDS from the solid solution. This equilibrium favors the precipitation of apatite and $Yb_{1.6}Gd_{0.4}Si_2O_7$. In addition to phase destabilization of this material via CMAS, the inwards diffusion of apatite and/or loss of the apatite layer after initial formation is of concern. Although the greater GdDS content may assist in mitigating CMAS infiltration into YbDS at shorter time scales, these results indicate that the performance of this material as a CMAS protective coating is not significantly improved over phase pure YbDS beyond 4 h.

Summary

A CMAS glass was deposited onto the surfaces of β-$Yb_{1.9}Gd_{0.1}Si_2O_7$, β-$Yb_{1.6}Gd_{0.4}Si_2O_7$, γ-$Yb_{1.4}Gd_{0.6}Si_2O_7$, γ-$Y_2Si_2O_7$ and β-$Yb_2Si_2O_7$ sintered pellets, and the mechanisms of reaction and infiltration were characterized for each material. While CMAS quickly infiltrated the grain boundaries of YbDS, a layer of apatite formed on the surface of YDS. Similarly, as GdDS content increased in the YbDS-GdDS solid solution, increased apatite formation was observed at the surface of these materials and the depth of CMAS infiltration was mitigated by up to ~60%. However, at longer time scales (≥4 h), both CMAS and the apatite reaction layer diffused inwards. Finally, it is important to note that although apatite layers formed on YDS, $Yb_{1.6}Gd_{0.4}Si_2O_7$, and $Yb_{1.4}Gd_{0.6}Si_2O_7$, the layer thicknesses were between 45 to 60 μm, which are quite large when considering the length scale of in-service deposited EBC topcoat materials (~250 to 300 μm). Therefore, utilizing GdDS to promote reactive crystallization in disilicate materials with a small RE cation may not be beneficial in the long term use of disilicate-based EBCs for next-generation engine components.

References

1. Lee KN. Current status of environmental barrier coatings for Si-based ceramics. *Surf Coatings Technol*. 2000;133–134:1–7. https://doi.org/10.1016/S0257-8972(00)00889-6
2. Lee KN, Fox DS, Bansal NP. Rare earth silicate environmental barrier coatings for SiC/SiC composites and Si3N4 ceramics. *J Eur Ceram Soc.* 2005;25(10):1705–1715. https://doi.org/10.1016/j.jeurceramsoc.2004.12.013
3. Xu Y, Hu X, Xu F, Li K. Rare earth silicate environmental barrier coatings: Present status and prospective. *Ceram Int.* 2017;43(8):5847–5855. https://doi.org/10.1016/j.ceramint.2017.01.153
4. Costa GCC, Jacobson NS. Mass spectrometric measurements of the silica activity in the Yb2O3-SiO2 system and implications to assess the degradation of silicate-based coatings in combustion environments. *J Eur Ceram Soc.* 2015;35(15):4259–4267. https://doi.org/10.1016/j.jeurceramsoc.2015.07.019
5. Jacobson NS. Silica Activity Measurements in the Y2O3-SiO2 System and Applications to Modeling of Coating Volatility. *J Am Ceram Soc.* 2014;97(6):1959–1965. https://doi.org/10.1111/jace.12974
6. Fernández-Carrión AJ, Allix M, Becerro AI. Thermal expansion of rare-earth pyrosilicates. *J Am Ceram Soc.* 2013;96(7):2298–2305. https://doi.org/10.1111/jace.12388
7. Lee KN. Environmental Barrier Coatings for SiCf/SiC. In: Bansal NP, Lamon J, eds. *Ceram. Matrix Compos. Mater. Model. Technol.* Hoboken, NJ: John Wiley and Sons, Inc.; 2014:430–451. https://doi.org/10.1002/9781118832998.ch15
8. Poerschke DL, Jackson RW, Levi CG. Silicate Deposit Degradation of Engineered Coatings in Gas Turbines: Progress Toward Models and Materials Solutions. *Annu Rev Mater Res.* 2017;47(1):297–330. https://doi.org/10.1146/annurev-matsci-010917-105000
9. Levi CG, Hutchinson JW, Vidal-Sétif M-H, Johnson CA. Environmental degradation of thermal-barrier coatings by molten deposits. *MRS Bull.* 2012;37(10):932–941. https://doi.org/10.1557/mrs.2012.230
10. Borom MP, Johnson CA, Peluso LA. Role of environmental deposits and operating surface temperature in spallation of air plasma sprayed thermal barrier coatings. *Surf Coatings Technol.* 1996;86–87:116–126.
11. Krämer S, Yang J, Levi CG, Johnson CA. Thermochemical interaction of thermal barrier coatings with molten CaO-MgO-Al2O3-SiO2 (CMAS) deposits. *J Am Ceram Soc.* 2006;89(10):3167–3175. https://doi.org/10.1111/j.1551-2916.2006.01209.x
12. Poerschke DL, Barth TL, Levi CG. Equilibrium relationships between thermal barrier oxides and silicate melts. *Acta Mater.* 2016;120:302–314. https://doi.org/10.1016/j.actamat.2016.08.077
13. Krämer S, Yang J, Levi CG. Infiltration-inhibiting reaction of gadolinium zirconate thermal barrier coatings with CMAS melts. *J Am Ceram Soc.* 2008;91(2):576–583. https://doi.org/10.1111/j.1551-2916.2007.02175.x
14. Aygun A, Vasiliev AL, Padture NP, Ma X. Novel thermal barrier coatings that are resistant to high-temperature attack by glassy deposits. *Acta Mater.* 2007;55(20):6734–6745. https://doi.org/10.1016/j.actamat.2007.08.028
15. Felsche J. Rare earth silicates with the apatite structure. *J Solid State Chem.* 1972;5(2):266–275. https://doi.org/10.1016/0022-4596(72)90039-4
16. Felsche J. The crystal chemistry of the rare-earth silicates. *Rare Earths. Struct. Bond.* Springer; 1973:99–197. https://doi.org/10.1007/3-540-06125-8_3

17. Stokes JL, Harder BJ, Wiesner VL, Wolfe DE. High-Temperature thermochemical interactions of molten silicates with Yb2Si2O7 and Y2Si2O7 environmental barrier coating materials. *J Eur Ceram Soc.* 2019;39(15):5059–5067. https://doi.org/10.1016/j.jeurceramsoc.2019.06.051
18. Stolzenburg F, Johnson MT, Lee KN, Jacobson NS, Faber KT. The interaction of calcium – magnesium – aluminosilicate with ytterbium silicate environmental barrier materials. *Surf Coat Technol.* 2015;284:44–50. https://doi.org/10.1016/j.surfcoat.2015.08.069
19. Poerschke DL, Hass DD, Eustis S, Seward GGE, Van Sluytman JS, Levi CG. Stability and CMAS resistance of ytterbium-silicate/hafnate EBCs/TBC for SiC composites. *J Am Ceram Soc.* 2015;98(1):278–286. https://doi.org/10.1111/jace.13262
20. Wiesner VL, Scales D, Johnson NS, Harder BJ, Garg A, Bansal NP. Calcium–magnesium aluminosilicate (CMAS) interactions with ytterbium silicate environmental barrier coating material at elevated temperatures. *Ceram Int.* 2020;46(10):16733–16742. https://doi.org/10.1016/j.ceramint.2020.03.249
21. Zhao H, Richards BT, Levi CG, Wadley HNG. Molten silicate reactions with plasma sprayed ytterbium silicate coatings. *Surf Coatings Technol.* 2016;288:151–162. https://doi.org/10.1016/j.surfcoat.2015.12.053
22. Turcer LR, Krause AR, Garces HF, Zhang L, Padture NP. Environmental-barrier coating ceramics for resistance against attack by molten calcia-magnesia-aluminosilicate (CMAS) glass: Part II, β-Yb2Si2O7 and β-Sc2Si2O7. *J Eur Ceram Soc.* 2018;38(11):3914–3924. https://doi.org/10.1016/j.jeurceramsoc.2018.03.010
23. Grant KM, Krämer S, Seward GGE, Levi CG. Calcium-magnesium alumino-silicate interaction with yttrium monosilicate environmental barrier coatings. *J Am Ceram Soc.* 2010;93(10):3504–3511. https://doi.org/10.1111/j.1551-2916.2010.03916.x
24. Poerschke DL, Levi CG. Effects of cation substitution and temperature on the interaction between thermal barrier oxides and molten CMAS. *J Eur Ceram Soc.* 2015;35(2):681–691. https://doi.org/10.1016/j.jeurceramsoc.2014.09.006
25. Poerschke DL, Seward GGE, Levi CG. Influence of Yb:Hf Ratio on Ytterbium Hafnate/Molten Silicate (CMAS) Reactivity. *J Am Ceram Soc.* 2016;99(2):651–659. https://doi.org/10.1111/jace.13964
26. Felsche J. Polymorphism and crystal data of the rare-earth disilicates of type R.E.2Si2O7. *J Less-Common Met.* 1970;21(1):1–14. https://doi.org/10.1016/0022-5088(70)90159-1
27. Turcer LR, Padture NP. Towards multifunctional thermal environmental barrier coatings (TEBCs) based on rare-earth pyrosilicate solid-solution ceramics. *Scr Mater.* 2018;154:111–117. https://doi.org/10.1016/j.scriptamat.2018.05.032
28. Turcer LR, Sengupta A, Padture NP. Low thermal conductivity in high-entropy rare-earth pyrosilicate solid-solutions for thermal environmental barrier coatings. *Scr Mater.* 2021;191:40–45. https://doi.org/10.1016/j.scriptamat.2020.09.008
29. Salanova A, Brummel IA, Yakovenko AA, Opila EJ, Ihlefeld JF. Phase stability and tensorial thermal expansion properties of single to high-entropy rare-earth disilicates. *J Am Ceram Soc.* 2023;106(5):3228–3238. https://doi.org/10.1111/jace.18986
30. Lv X, Cui J, Zhang J, Wang J. Phase composition and property evolution of (Yb1−xHox)2Si2O7 solid solution as environmental/thermal barrier coating candidates. *J Eur Ceram Soc.* 2022;(April):1–11. https://doi.org/10.1016/j.jeurceramsoc.2022.04.020
31. He Y, Wang X, Wang C, et al. Significantly improved corrosion resistance of high-entropy rare-earth silicate multiphase ceramics against molten CMAS. *J Am Ceram Soc.* 2023;106(5):2744–2751. https://doi.org/10.1111/jace.18999

32. Chen Z, Lin C, Zheng W, et al. Mechanism of enhanced corrosion resistance against molten CMAS for pyrosilicates by high-entropy design. *J Am Ceram Soc.* 2023;106(10):6000–6013. https://doi.org/10.1111/jace.19192
33. Stokes JL, Harder BJ, Wiesner VL, Wolfe DE. Crystal structures and thermal expansion of Yb2Si2O7–Gd2Si2O7 solid solutions. *J Solid State Chem.* 2022;312(March):123166. https://doi.org/10.1016/j.jssc.2022.123166
34. Stokes JL, Harder BJ, Wiesner VL, Wolfe DE. Melting and Crystallization Behavior of CaO-MgO-Al2O3-SiO2 Silicates Relevant to Turbine Engine Applications. NASA/TM-20210020388 https://ntrs.nasa.gov/citations/20210020388. 2021.
35. Harder BJ, Stokes JL, Kowalski BA, Stuckner J, Setlock JA. Steam oxidation performance of Yb2Si2O7 environmental barrier coatings exposed to CMAS. *J Eur Ceram Soc.* 2024;44(4):2486–2498. https://doi.org/10.1016/j.jeurceramsoc.2023.10.073
36. Stokes JL, Presby MJ, Webster RI, Setlock J, Harder BJ. Thermochemical/Thermomechanical Synergies in High-Temperature Solid Particle Erosion of CMAS-Exposed EBCs. *Proc. ASME Turbo Expo 2023 Turbomach. Tech. Conf. Expo.* American Society of Mechanical Engineers; 2023 https://doi.org/10.1115/GT2023-101212
37. Fedorov NF, Andreev IF, Meliksetyan NS. Preparation and Properties of Single Crystals of Silicate-Oxyapatites CaLn4(SiO4)3O. *Inorg Mater.* 1975;11:1137.
38. Summers WD, Poerschke DL, Park D, Shaw JH, Zok FW, Levi CG. Roles of composition and temperature in silicate deposit-induced recession of yttrium disilicate. *Acta Mater.* 2018;160:34–46. https://doi.org/10.1016/j.actamat.2018.08.043
39. Wiesner VL, Harder BJ, Bansal NP. High-temperature interactions of desert sand CMAS glass with yttrium disilicate environmental barrier coating material. *Ceram Int.* 2018;44(18):22738–22743. https://doi.org/10.1016/j.ceramint.2018.09.058
40. Poerschke DL, Shaw JH, Verma N, Zok FW, Levi CG. Interaction of yttrium disilicate environmental barrier coatings with calcium-magnesium-iron alumino-silicate melts. *Acta Mater.* 2018;145:451–461. https://doi.org/10.1016/j.actamat.2017.12.004
41. Costa G, Harder BJ, Bansal NP, Kowalski BA, Stokes JL. Thermochemistry of calcium rare-earth silicate oxyapatites. *J Am Ceram Soc.* 2020;103(2):1446–1453. https://doi.org/10.1111/jace.16816
42. Stokes JL, Harder BJ, Wiesner VL, Wolfe DE. Effects of crystal structure and cation size on molten silicate reactivity with environmental barrier coating materials. *J Am Ceram Soc.* 2020;103(1):622–634. https://doi.org/10.1111/jace.16694